

Surface-plasmon-polariton wave propagation guided by a metal slab in a sculptured nematic thin film

Muhammad Faryad and Akhlesh Lakhtakia[‡]

Nanoengineered Metamaterials Group (NanoMM), Department of Engineering Science and Mechanics, Pennsylvania State University, University Park, PA 16802-6812, USA

E-mail: akhlesh@psu.edu

Abstract.

Surface-plasmon-polariton (SPP) wave propagation guided by a metal slab in a periodically nonhomogeneous sculptured nematic thin film (SNTF) was studied theoretically. The morphologically significant planes of the SNTF on both sides of the metal slab could either be aligned or twisted with respect to each other. The canonical boundary-value problem was formulated, solved for SPP-wave propagation, and examined to determine the effect of slab thickness on the multiplicity and the spatial profiles of SPP waves. Decrease in slab thickness was found to result in more intense coupling of two metal/SNTF interfaces. But when the metal slab becomes thicker, the coupling between the two interfaces reduces and SPP waves localize to one of the two interfaces. The greater the coupling between the two metal/SNTF interfaces, the smaller is the phase speed.

Keywords: sculptured thin film, surface plasmon polariton

[‡] Corresponding author

1. Introduction

Quasi-particles formed collectively by plasmons and polaritons bound to the interface of a metal and a dielectric material are called surface plasmon-polaritons (SPPs) [1, 2, 3, 4]. Although SPPs are quantum objects, trains of SPPs traveling along the interface are classically viewed as SPP waves. Much recent literature is devoted to the exploitation of SPP waves for diverse technological purposes, including sensing, imaging, and communications [5, 6, 7, 8].

This technoscientific ferment is due to a resonance phenomenon that arises when the energy carried by photons in the dielectric material is transferred to free electrons in the metal at that interface, and vice versa. Different dielectric materials will become differently polarized on interrogation by an electromagnetic field, thereby enabling a widely used technique for sensing chemicals and biochemicals [5, 7]. Furthermore, SPP imaging systems are used for high-throughput analysis of biomolecular interactions—for proteomics, drug discovery, and pathway elucidation [9, 10]. SPP-based imaging technology has been successfully applied to the screening of bioaffinity interactions with DNA, carbohydrates, peptides, phage display libraries, and proteins [11]. SPP-based imaging techniques are also going to be useful for lithography [2, 12]. Finally, as SPP waves can be excited in the terahertz and optical regimes, they may be useful for high-speed information on computer chips [13]. Whereas conventional wires are very attenuative at frequencies beyond a few tens of GHz, ohmic losses are minimal for plasmonic transmission [8] which enables long-range communications [14].

Even a cursory perusal of literature will show that only one SPP wave at a specific frequency is excited along the interface, if the partnering dielectric material is homogeneous. But if this material were to be periodically nonhomogeneous in the direction normal to the interface, the number of SPP waves—of different phase speeds, attenuation rates, and field structures, but the same frequency—can be higher. The material can be isotropic [15] or anisotropic [16, 17], the latter obviously providing more options due to birefringence [18]. The possibility of exciting multiple SPP waves provides exciting prospects for enhancing the scope of the applications of SPP waves. For sensing applications, the use of more than one distinct SPP waves would increase confidence in a reported measurement; also, more than one analyte could be sensed at the same time, thereby increasing the capabilities of multi-analyte sensors. For imaging applications, the simultaneous creation of two images may become possible. For plasmonic communications, the availability of multiple channels would make information transmission more reliable as well as enhance capacity.

These possibilities are promised by the use of sculptured thin films (STFs) as the partnering dielectric material. STFs are anisotropic and unidirectionally nonhomogeneous thin films whose permittivity profile has been nanoengineered during the physical vapor deposition process [19, 20]. The possibility of multiple SPP waves localized to the single interface of a metal and a periodically nonhomogeneous sculptured nematic thin film (SNTF) has been demonstrated both theoretically [17, 21, 22] and

experimentally [23]. An SNTF is a special type of an STF—with a permittivity profile which is sculptured, during physical vapor deposition, only in one plane called the morphologically significant plane [20]. Also, SPP wave propagation along the interface of a metal and a chiral STF has also been shown both theoretically [24] and experimentally [25] to admit more than one type of SPP waves.

A further increase in the number of SPP waves would require the use of multiple parallel metal/dielectric interfaces, which is already established well with isotropic dielectric materials [26, 27, 28]. Pursuing this line of thinking, we decided to solve the canonical problem of wave propagation localized to a sufficiently thin metallic slab inserted in an SNTF. As our supposition was confirmed in a preliminary study [29], we conducted a full-scale investigation, the details and the results of which are reported here. In Sec. 2, we present the theoretical formulation of the canonical boundary-value problem, where a dispersion equation is obtained. Representative numerical results are discussed in Sec. 3, and concluding remarks are given in Sec. 4.

An $\exp(-i\omega t)$ time-dependence is implicit, with ω denoting the angular frequency, t the time, and $i = \sqrt{-1}$. The free-space wavenumber, the free-space wavelength, and the intrinsic impedance of free space are denoted by $k_0 = \omega\sqrt{\varepsilon_0\mu_0}$, $\lambda_0 = 2\pi/k_0$, and $\eta_0 = \sqrt{\mu_0/\varepsilon_0}$, respectively, with μ_0 and ε_0 being the permeability and permittivity of free space. Vectors are in boldface, dyadics are underlined twice, column vectors are in boldface and enclosed within square brackets, and matrixes are underlined twice and square-bracketed. The asterisk denotes the complex conjugate, and the Cartesian unit vectors are identified as $\hat{\mathbf{u}}_x$, $\hat{\mathbf{u}}_y$, and $\hat{\mathbf{u}}_z$.

2. Canonical Boundary-Value Problem

Suppose that the region $L_- \leq z \leq L_+$ is occupied by an isotropic and homogeneous metal with complex-valued relative permittivity scalar ε_{met} . The thickness of the metal slab is denoted by $L_{met} = L_+ - L_-$.

The regions $z \gtrless L_{\pm}$ are occupied by the chosen SNTF with periodically nonhomogeneous permittivity dyadic [17, 21]

$$\underline{\underline{\varepsilon}}_{SNTF}(z) = \varepsilon_0 \underline{\underline{S}}_z(\gamma^{\pm}) \cdot \underline{\underline{S}}_y(z) \cdot \underline{\underline{\varepsilon}}_{ref}(z) \cdot \underline{\underline{S}}_y^{-1}(z) \cdot \underline{\underline{S}}_z^{-1}(\gamma^{\pm}), \quad z \gtrless L_{\pm}, \quad (1)$$

where the locally orthorhombic symmetry is expressed through the diagonal dyadic

$$\underline{\underline{\varepsilon}}_{ref}(z) = \varepsilon_a(z) \hat{\mathbf{u}}_z \hat{\mathbf{u}}_z + \varepsilon_b(z) \hat{\mathbf{u}}_x \hat{\mathbf{u}}_x + \varepsilon_c(z) \hat{\mathbf{u}}_y \hat{\mathbf{u}}_y \quad (2)$$

and the local tilt dyadic

$$\underline{\underline{S}}_y(z) = (\hat{\mathbf{u}}_x \hat{\mathbf{u}}_x + \hat{\mathbf{u}}_z \hat{\mathbf{u}}_z) \cos[\chi(z)] + (\hat{\mathbf{u}}_z \hat{\mathbf{u}}_x - \hat{\mathbf{u}}_x \hat{\mathbf{u}}_z) \sin[\chi(z)] + \hat{\mathbf{u}}_y \hat{\mathbf{u}}_y \quad (3)$$

expresses nematicity. Both the relative permittivity scalars $\varepsilon_{a,b,c}(z)$ and the tilt angle $\chi(z)$ are supposed to have been nano-engineered by a periodic variation of the direction of the vapor flux during fabrication by physical vapor deposition [20, 23]. This periodic variation is captured by the vapor incidence angle [23]

$$\chi_v(z) = \tilde{\chi}_v \pm \delta_v \sin \left[\frac{\pi(z - L_{\pm})}{\Omega} \right], \quad z \gtrless L_{\pm}, \quad (4)$$

that varies sinusoidally with z . The third dyadic in Eq. (1) was chosen as

$$\underline{\underline{S}}_z(\gamma^\pm) = (\hat{\mathbf{u}}_x \hat{\mathbf{u}}_x + \hat{\mathbf{u}}_y \hat{\mathbf{u}}_y) \cos \gamma^\pm + (\hat{\mathbf{u}}_y \hat{\mathbf{u}}_x - \hat{\mathbf{u}}_x \hat{\mathbf{u}}_y) \sin \gamma^\pm + \hat{\mathbf{u}}_z \hat{\mathbf{u}}_z, \quad (5)$$

so that plane formed by the unit vectors $\hat{\mathbf{u}}_z$ and $\hat{\mathbf{u}}_x \cos \gamma^\pm + \hat{\mathbf{u}}_y \sin \gamma^\pm$ is the morphologically significant plane for $z \gtrless L_\pm$. Thus, there is sufficient flexibility in the formulation with respect to the twist $\gamma^+ - \gamma^-$ of the two morphologically significant planes. Note that $\gamma^+ = \gamma^-$ in our preliminary report [29], but that restriction was removed for the full-scale investigations reported here.

Without loss of generality, let us choose the direction of SPP-wave propagation in the xy plane to be parallel to the x axis. Accordingly, we set

$$\left. \begin{aligned} \mathbf{E}(\mathbf{r}) &= \mathbf{e}(z) \exp(i\kappa x) \\ \mathbf{H}(\mathbf{r}) &= \mathbf{h}(z) \exp(i\kappa x) \end{aligned} \right\}, \quad (6)$$

where κ is a complex-valued scalar.

The axial field components $e_z(z)$ and $h_z(z)$ can be expressed in terms of the column vector

$$[\mathbf{f}(z)] = [e_x(z) \quad e_y(z) \quad h_x(z) \quad h_y(z)]^T \quad (7)$$

via

$$\kappa \begin{bmatrix} e_z(z) \\ 0 \\ h_z(z) \\ 0 \end{bmatrix} = \begin{cases} \underline{\underline{A}}^\pm(z) \cdot [\mathbf{f}(z)], & z \gtrless L_\pm, \\ \underline{\underline{A}}^{met}(z) \cdot [\mathbf{f}(z)], & z \in (L_-, L_+) , \end{cases} \quad (8)$$

where one 4×4 matrix

$$\begin{aligned} \underline{\underline{A}}^\pm(z) &= \begin{bmatrix} 0 & 0 & 0 & -\frac{\kappa^2}{\omega \varepsilon_0} \frac{\varepsilon_d(z)}{\varepsilon_a(z) \varepsilon_b(z)} \\ 0 & 0 & 0 & 0 \\ 0 & \frac{\kappa^2}{\omega \mu_0} & 0 & 0 \\ 0 & 0 & 0 & 0 \end{bmatrix} \\ &+ \kappa \frac{\varepsilon_d(z) [\varepsilon_a(z) - \varepsilon_b(z)]}{\varepsilon_a(z) \varepsilon_b(z)} \begin{bmatrix} \sin[\chi(z)] & \cos[\chi(z)] & 0 & 0 \\ \cos \gamma^\pm & \sin \gamma^\pm & 0 & 0 \\ 0 & 0 & 0 & 0 \\ 0 & 0 & 0 & -\sin \gamma^\pm \\ 0 & 0 & 0 & \cos \gamma^\pm \end{bmatrix} \end{aligned} \quad (9)$$

involves the auxiliary quantity

$$\varepsilon_d(z) = \varepsilon_a(z) \varepsilon_b(z) / \{ \varepsilon_a(z) \cos^2[\chi(z)] + \varepsilon_b(z) \sin^2[\chi(z)] \}, \quad (10)$$

and the other 4×4 matrix

$$\underline{\underline{A}}^{met}(z) = \begin{bmatrix} 0 & 0 & 0 & -\frac{\kappa^2}{\omega \varepsilon_0 \varepsilon_{met}} \\ 0 & 0 & 0 & 0 \\ 0 & \frac{\kappa^2}{\omega \mu_0} & 0 & 0 \\ 0 & 0 & 0 & 0 \end{bmatrix}. \quad (11)$$

The column vector $[\mathbf{f}(z)]$ satisfies the matrix differential equations

$$\frac{d}{dz} [\mathbf{f}(z)] = i [\underline{\underline{P}}^\pm(z)] \cdot [\mathbf{f}(z)] , \quad z \gtrless L_\pm , \quad (12)$$

and

$$\frac{d}{dz} [\mathbf{f}(z)] = i [\underline{\underline{P}}^{met}(z)] \cdot [\mathbf{f}(z)] , \quad z \in (L_-, L_+) , \quad (13)$$

where the 4×4 matrixes

$$\begin{aligned} [\underline{\underline{P}}^\pm(z)] &= [\underline{\underline{A}}^\pm(z)] + \\ \omega &\begin{bmatrix} 0 & 0 & 0 & \mu_0 \\ 0 & 0 & -\mu_0 & 0 \\ \varepsilon_0 [\varepsilon_c(z) - \varepsilon_d(z)] \cos \gamma^\pm \sin \gamma^\pm & -\varepsilon_0 [\varepsilon_c(z) \cos^2 \gamma^\pm + \varepsilon_d(z) \sin^2 \gamma^\pm] & 0 & 0 \\ \varepsilon_0 [\varepsilon_c(z) \sin^2 \gamma^\pm + \varepsilon_d(z) \cos^2 \gamma^\pm] & -\varepsilon_0 [\varepsilon_c(z) - \varepsilon_d(z)] \cos \gamma^\pm \sin \gamma^\pm & 0 & 0 \end{bmatrix} \end{aligned} \quad (14)$$

and

$$[\underline{\underline{P}}^{met}(z)] = [\underline{\underline{A}}^{met}(z)] + \omega \begin{bmatrix} 0 & 0 & 0 & \mu_0 \\ 0 & 0 & -\mu_0 & 0 \\ 0 & -\varepsilon_0 \varepsilon_{met} & 0 & 0 \\ \varepsilon_0 \varepsilon_{met} & 0 & 0 & 0 \end{bmatrix} . \quad (15)$$

Equation (13) can be solved straightforwardly to yield

$$[\mathbf{f}(L_+)] = \exp \{ i [\underline{\underline{P}}^{met}] (L_+ - L_-) \} \cdot [\mathbf{f}(L_-)] . \quad (16)$$

Equation (12) requires numerical solution by the piecewise uniform approximation technique [22, 30]. The ultimate aim is to determine the matrixes $[\underline{\underline{Q}}^\pm]$ that appear in the relations

$$[\mathbf{f}(L_\pm \pm 2\Omega)] = [\underline{\underline{Q}}^\pm] \cdot [\mathbf{f}(L_\pm)] \quad (17)$$

to characterize the optical response of one period of the SNTF on either side of the metal slab. Basically, this technique consists of subdividing each period of the SNTF into a cascade of electrically thin sublayers parallel to the plane $z = 0$, and assuming the dielectric properties to be spatially uniform in each sublayer. A sufficiently large number $N + 1$ points $z_n^\pm = L_\pm \pm 2\Omega (n/N)$, $n \in [0, N]$, are defined on each side of the metal slab and the matrixes

$$[\underline{\underline{W}}_n^\pm] = \exp \left\{ \pm i \left[\underline{\underline{P}}^\pm \left(\frac{z_{n-1}^\pm + z_n^\pm}{2} \right) \right] \frac{2\Omega}{N} \right\} , \quad n \in [1, N] , \quad (18)$$

are calculated for a specific value of κ ; then

$$[\underline{\underline{Q}}^\pm] \cong [\underline{\underline{W}}_N^\pm] \cdot [\underline{\underline{W}}_{N-1}^\pm] \cdot \dots \cdot [\underline{\underline{W}}_2^\pm] \cdot [\underline{\underline{W}}_1^\pm] . \quad (19)$$

A sublayer thickness $2\Omega/N = 2$ nm was adequate for the results reported in Sec. 3.

By virtue of the Floquet–Lyapunov theorem [31], we can define the matrixes $[\underline{\underline{Q}}^\pm]$ such that

$$[\underline{\underline{Q}}^\pm] = \exp \left\{ \pm i 2\Omega [\underline{\underline{Q}}^\pm] \right\} . \quad (20)$$

Both $[\underline{Q}^\pm]$ and $[\underline{\tilde{Q}}^\pm]$ share the same eigenvectors, and their eigenvalues are also related as follows. Let $[\mathbf{t}^\pm]^{(n)}$, $n \in [1, 4]$, be the eigenvector corresponding to the n th eigenvalue σ_n^\pm of $[\underline{Q}^\pm]$; then, the corresponding eigenvalue α_n^\pm of $[\underline{\tilde{Q}}^\pm]$ is given by

$$\alpha_n^\pm = \mp i \frac{\ln \sigma_n^\pm}{2\Omega}. \quad (21)$$

The electromagnetic fields of the SPP wave must diminish in magnitude as $z \rightarrow \pm\infty$. Therefore, in the half-space $z > L_+$, we first label the eigenvalues of $[\underline{\tilde{Q}}^+]$ such that $\text{Im}[\alpha_{1,2}^+] > 0$ and then set

$$[\mathbf{f}(L_+)] = \begin{bmatrix} [\mathbf{t}^+]^{(1)} & [\mathbf{t}^+]^{(2)} \end{bmatrix} \cdot \begin{bmatrix} A_1^+ \\ A_2^+ \end{bmatrix}, \quad (22)$$

where $A_{1,2}^+$ are unknown scalars; the other two eigenvalues of $[\underline{\tilde{Q}}^+]$ describe fields that amplify as $z \rightarrow +\infty$ and cannot therefore contribute to the SPP wave. A similar argument for the half-space $z < L_-$ requires us to ensure that $\text{Im}[\alpha_{1,2}^-] < 0$ and then to set

$$[\mathbf{f}(L_-)] = \begin{bmatrix} [\mathbf{t}^-]^{(1)} & [\mathbf{t}^-]^{(2)} \end{bmatrix} \cdot \begin{bmatrix} A_1^- \\ A_2^- \end{bmatrix}, \quad (23)$$

where $A_{1,2}^-$ are unknown scalars.

Combining Eqs. (16), (22), and (23), we obtain a matrix equation which may be rearranged as

$$[\underline{M}(\kappa)] \cdot \begin{bmatrix} A_1^+ \\ A_2^+ \\ A_1^- \\ A_2^- \end{bmatrix} = \begin{bmatrix} 0 \\ 0 \\ 0 \\ 0 \end{bmatrix}. \quad (24)$$

For a nontrivial solution, the 4×4 matrix $[\underline{M}(\kappa)]$ must be singular, so that

$$\det [\underline{M}(\kappa)] = 0 \quad (25)$$

is the dispersion equation for SPP-wave propagation.

3. Numerical Results and Discussion

A MathematicaTM program was written and implemented to solve (25) to obtain κ for specific values of γ^+ and γ^- . The dispersion equation (25) was solved using the Newton-Raphson technique [33] for three different values of the twist between the morphologically significant planes on either side of the metal slab; we chose

- (i) $\gamma^- = \gamma^+$,
- (ii) $\gamma^- = \gamma^+ + 90^\circ$, and
- (iii) $\gamma^- = \gamma^+ + 45^\circ$,

while γ^+ was kept as a variable. For each choice, the boundaries of the metal slab were taken to be at $L_{\pm} = \pm 7.5, \pm 12.5, \pm 25, \text{ or } \pm 45$ nm. These selections adequately represent the results of our investigation.

The free-space wavelength was fixed at $\lambda_0 = 633$ nm for all calculations. The metal was taken to be bulk aluminum ($\varepsilon_{met} = -56 + 21i$). The skin depth of aluminum at the chosen wavelength is $\Delta_{met} = \{\text{Im}[k_0\sqrt{\varepsilon_{met}}]\}^{-1} = 13.24$ nm, a quantity of interest in relation to the thickness of the metal slab. The SNTF was chosen to be made of titanium oxide [29, 32], with

$$\left. \begin{aligned} \varepsilon_a(z) &= [1.0443 + 2.7394v(z) - 1.3697v^2(z)]^2 \\ \varepsilon_b(z) &= [1.6765 + 1.5649v(z) - 0.7825v^2(z)]^2 \\ \varepsilon_c(z) &= [1.3586 + 2.1109v(z) - 1.0554v^2(z)]^2 \\ \chi(z) &= \tan^{-1}[2.8818 \tan \chi_v(z)] \end{aligned} \right\}, \quad (26)$$

where $v(z) = 2\chi_v(z)/\pi$. The angles $\tilde{\chi}_v$ and δ_v were taken to be 45° and 30° , respectively, for all results presented here.

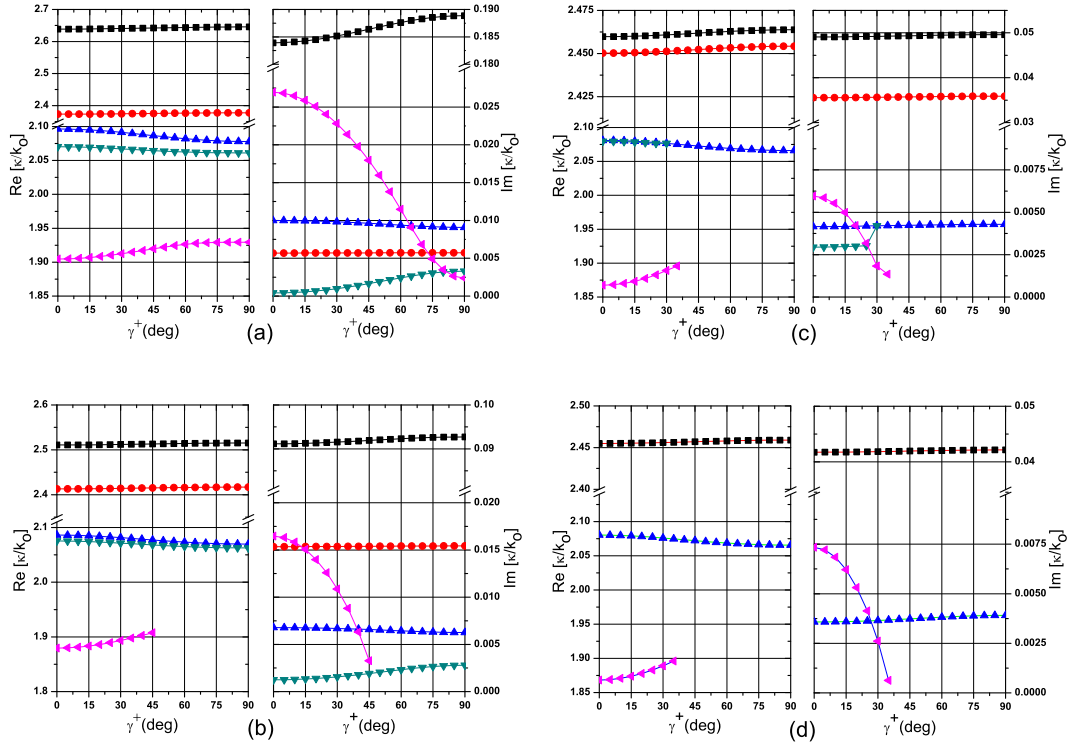


Figure 1. Variation of real and imaginary parts of κ/k_0 with γ^+ , when $\gamma^- = \gamma^+$. (a) $L_{\pm} = \pm 7.5$ nm, (b) $L_{\pm} = \pm 12.5$ nm, (c) $L_{\pm} = \pm 25$ nm, and (d) $L_{\pm} = \pm 45$ nm.

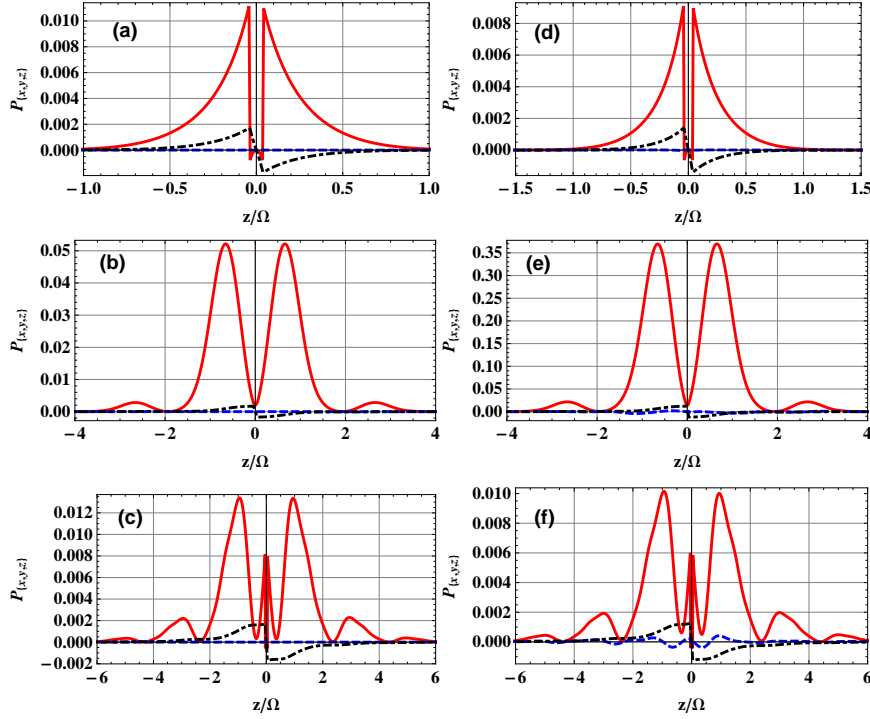


Figure 2. Variation of the Cartesian components of the time-averaged Poynting vector $\mathbf{P}(x, z)$ along the z axis when $x = 0$, $L_{\pm} = \pm 7.5$ nm, and $\gamma^- = \gamma^+$. (a-c) $\gamma^+ = 0$, and (d-f) $\gamma^+ = 25^\circ$. (a) $\kappa/k_0 = 2.6387 + i0.1839$, (b) $\kappa/k_0 = 2.0964 + i0.009997$, (c) $\kappa/k_0 = 1.9048 + i0.02696$, (d) $\kappa/k_0 = 2.6399 + i0.1848$, (e) $\kappa/k_0 = 2.09285 + i0.00988$, and (f) $\kappa/k_0 = 1.9103 + i0.02405$. The x -, y - and z -directed components of $\mathbf{P}(x, z)$ are represented by solid red, dashed blue, and chain-dashed black lines, respectively.

3.1. $\gamma^- = \gamma^+$

Let us begin with the case when the morphologically significant planes of the SNTF on both sides of the metal slab are aligned with each other and make an angle $\gamma^- = \gamma^+$ with respect to the direction of SPP-wave propagation in the xy plane. This case had been briefly studied in a predecessor communication [29], but is now discussed in detail.

The real and imaginary parts of κ/k_0 which satisfies Eq. (25) are presented in Fig. 1 as functions of $\gamma^+ \in [0^\circ, 90^\circ]$; by virtue of symmetry, the solutions for $180^\circ + \gamma^+$ and $360^\circ - \gamma^+$ are the same as for γ^+ . For the thinnest metal slab ($L_{\pm} = \pm 7.5$ nm), the solutions are organized in five branches which span the entire range of γ^+ . As the metal slab thickens to 25 nm ($L_{\pm} = \pm 12.5$ nm), the number of branches does not change, but only four of those branches span the entire range of γ^+ and one is confined to $\gamma^+ \in [0^\circ, 49^\circ]$. Further thickening of the metal slab to 50 nm ($L_{\pm} = \pm 25$ nm) leads to five values of κ satisfying the dispersion equation only in the range $\gamma^+ \in [0^\circ, 35^\circ]$, four in the range $\gamma^+ \in (35^\circ, 37^\circ]$, and three in the range $\gamma^+ \in (37^\circ, 90^\circ]$. Finally, for a 90-nm thick metal slab ($L_{\pm} = \pm 45$ nm) only three solutions exist for $\gamma \in [0^\circ, 36^\circ]$ and two for $\gamma \in (36^\circ, 90^\circ]$, these solutions being the same as for a single metal/SNTF interface [22]. We conclude that, as the thickness of the metal slab is increased, the coupling between

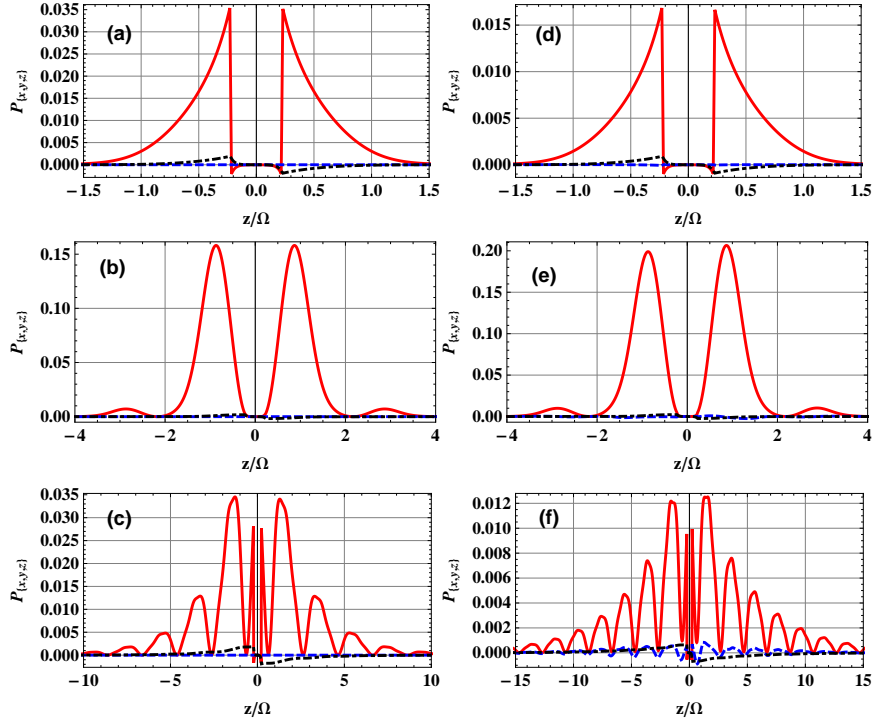


Figure 3. Same as Fig. 2 except for $L_{\pm} = \pm 45$ nm. (a) $\kappa/k_0 = 2.4549 + i0.04173$, (b) $\kappa/k_0 = 2.08034 + i0.003574$, (c) $\kappa/k_0 = 1.8683 + i0.00734$, (d) $\kappa/k_0 = 2.4557 + i0.04181$, (e) $\kappa/k_0 = 2.0773 + i0.00363$, and (f) $\kappa/k_0 = 1.8830 + i0.00413$.

two metal/SNTF interfaces $z = L_-$ and $z = L_+$ decreases; ultimately, the two interfaces decouple from each other when the thickness L_{met} significantly exceeds twice the skin depth Δ_{met} in the metal.

The solutions in Fig. 1 can be categorized into three sets. The first set comprises those solutions for which $\text{Re}[\kappa/k_0]$ lies between 2.3 and 2.7. This set has two branches when the metal slab is 15-nm thick, both branches spanning the entire range of γ^+ . As the thickness L_{met} increases, the two branches come closer to each other and eventually merge completely. The second set comprises solutions for which $\text{Re}[\kappa/k_0]$ lies between 2.05 and 2.1. It also has two branches when $L_{met} = 15$ nm, both branches coalescing into one branch as the thickness increases. Complete merger of the two branches of the first set occurs at a value of L_{met} smaller than that for the two branches of the second set. Regardless of the value of L_{met} , solutions in the second set can be found over the entire range of γ^+ . The third set consists of solutions lying on just one branch ($1.85 < \text{Re}[\kappa/k_0] < 1.95$), but the maximum value of γ^+ on this branch decreases rapidly from 90° as L_{met} increases from 15 nm.

The foregoing categorization is also meaningful as the spatial profiles of the fields are very similar for both solutions (for a specific value of γ^+) in the first two sets. The same remark can be made for the spatial profiles of the time-averaged Poynting vector

$$\mathbf{P}(x, z) = \frac{1}{2} \text{Re} [\mathbf{E}(x, z) \times \mathbf{H}^*(x, z)] . \quad (27)$$

Representative plots of $\mathbf{P}(0, z)$ against z are presented in Figs. 2 and 3 for combinations of (i) three values of κ , one from each set, and (ii) two values of γ^+ . Whereas $\gamma^+ = 0$ was chosen because it represents the propagation of SPP waves in the morphologically significant plane of the SNTF on either side of the metal slab, $\gamma^+ = 25^\circ$ was chosen for the direction of SPP-wave propagation oblique to that plane.

Figure 2 shows the spatial profiles of $\mathbf{P}(0, z)$ for $L_\pm = \pm 7.5$ nm. The chosen values of κ/k_0 are: (a) $2.6387 + i0.1839$, (b) $2.0964 + i0.009997$, and (c) $1.9048 + i0.02696$ for $\gamma^+ = 0$; and (d) $2.6399 + i0.1848$, (e) $2.09285 + i0.00988$, and (f) $1.9103 + i0.02405$ for $\gamma^+ = 25^\circ$. In order to determine these profiles, first A_1^+ was set equal to unity and then the remaining coefficients were found using Eq. (24) for all κ/k_0 —except for $\kappa/k_0 = 2.0964 + i0.009997$, for which $A_2^+ = 1$ was set and the remaining coefficients were found using Eq. (24). The spatial profiles shown allow us to conclude that

- (i) the SPP waves are bound strongly to both metal/SNTF interfaces, and
- (ii) the power density mostly resides in the SNTF.

Representative calculated values of the penetration depth Δ_z^\pm of the SPP wave into the metal, defined as the distance along the z axis (in the metal slab) at which the amplitude of the electric or magnetic field decays to e^{-1} of its value at the nearest metal/SNTF interface $z = L_\pm$, are tabulated in Table 1 for $L_\pm = \pm 7.5$ nm. The penetration depths for all SPP waves are ~ 12.7 nm, which confirms strong coupling of the two metal/SNTF interfaces. This is not surprising since $\Delta_z^- = \Delta_z^+$ is very close to Δ_{met} .

Table 1. Penetration depths $\Delta_z^+ = \Delta_z^-$ for $L_\pm = \pm 7.5$ nm and $\gamma^- = \gamma^+$. The solutions are numbered in descending values of $\text{Re}[\kappa/k_0]$.

$\Delta_z^+ = \Delta_z^-$ (nm)					
$\gamma^+ = \gamma^-$	Solution				
	1st	2nd	3rd	4th	5th
0°	12.5458	12.6558	12.7780	12.7882	12.8564
15°	12.5456	12.6557	12.7786	12.7886	12.8555
30°	12.5450	12.6553	12.7801	12.7896	12.8532
45°	12.5443	12.6548	12.7821	12.7907	12.8500
60°	12.5436	12.6543	12.7839	12.7916	12.8470
75°	12.5431	12.6539	12.7852	12.7921	12.8454
90°	12.5430	12.6538	12.7857	12.7922	12.8451

The spatial profiles of $\mathbf{P}(0, z)$ for $L_\pm = \pm 45$ nm are presented in Fig. 3 for six selected values of κ/k_0 identified in the figure caption. These profiles were obtained after A_1^+ was set equal to unity, except that $A_2^+ = 1$ was used for $\kappa/k_0 = 2.08034 + i0.003574$. The spatial profiles of $\mathbf{P}(0, z)$ for $L_\pm = \pm 12.5$ nm and ± 25 nm have not been shown here because the spatial profiles for these cases are similar to those shown in Figs. 2 and

3. Representative values of the penetration depths Δ_z^\pm for $L_\pm = \pm 45$ nm are given in Table 2. The penetration depths for this case are of the same order as for $L_\pm = \pm 7.5$ nm. As the thickness of the metal slab is 90 nm, it can be safely concluded that the SPP waves propagating on the two metal/SNTF interfaces are not coupled to each other but are propagating independently.

Table 2. Penetration depths $\Delta_z^+ = \Delta_z^-$ for $L_\pm = \pm 45$ nm and $\gamma^- = \gamma^+$. The solutions are numbered in descending values of $\text{Re}[\kappa/k_0]$.

$\Delta_z^+ = \Delta_z^-$ (nm)			
$\gamma^+ = \gamma^-$	Solution		
	1st	2nd	3rd
0°	12.6206	12.7843	12.8691
15°	12.6205	12.7848	12.8669
30°	12.6201	12.7860	12.8608
45°	12.6196	12.7877	
60°	12.6192	12.7891	
75°	12.6188	12.7901	
90°	12.6187	12.7904	

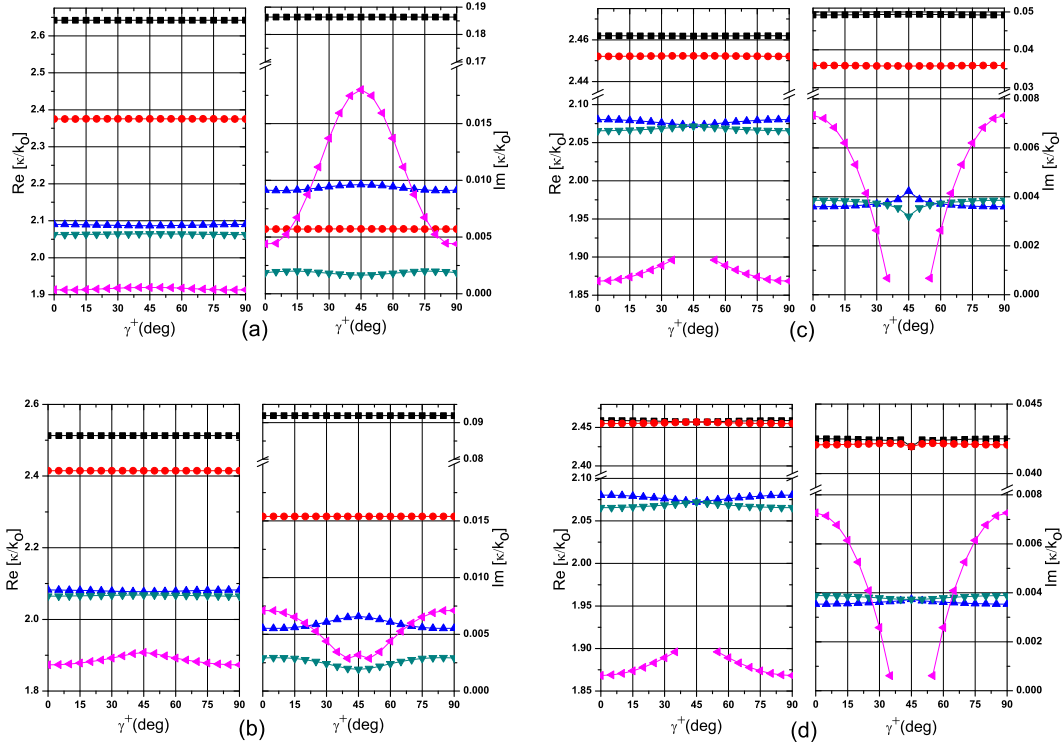


Figure 4. Same as Fig. 1 except that $\gamma^- = \gamma^+ + 90^\circ$.

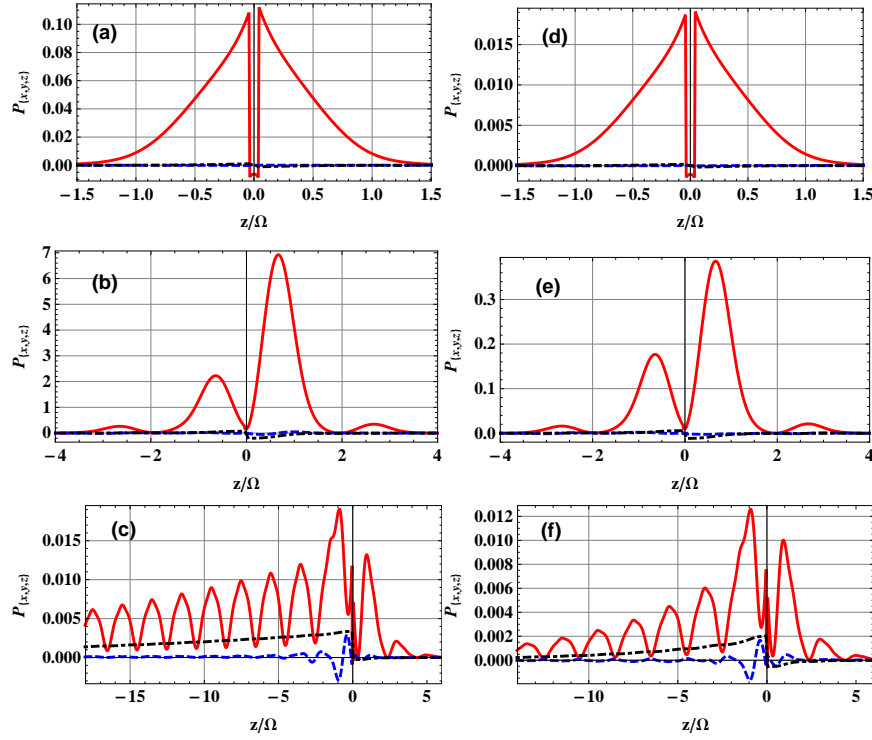


Figure 5. Variation of the Cartesian components of the time-averaged Poynting vector $\mathbf{P}(x, z)$ along the z axis when $x = 0$, $L_{\pm} = \pm 7.5$ nm, and $\gamma^- = \gamma^+ + 90^\circ$. (a-c) $\gamma^+ = 0$, and (d-f) $\gamma^+ = 25^\circ$. The following values of κ were chosen for rough correspondence with those in Fig. 2: (a) $\kappa/k_0 = 2.3753 + i0.005699$, (b) $\kappa/k_0 = 2.09013 + i0.009135$, (c) $\kappa/k_0 = 1.9133 + i0.004397$, (d) $\kappa/k_0 = 2.3756 + i0.005713$, (e) $\kappa/k_0 = 2.08797 + i0.009324$, and (f) $\kappa/k_0 = 1.9165 + i0.01117$.

3.2. $\gamma^- = \gamma^+ + 90^\circ$

The real and imaginary parts of κ/k_0 that satisfies the dispersion equation (25) for $\gamma^- = \gamma^+ + 90^\circ$ are given in Fig. 4 as functions of $\gamma^+ \in [0^\circ, 90^\circ]$. Due to the symmetry of the problem, the solutions for $90^\circ \pm \gamma^+$, $180^\circ \pm \gamma^+$, $270^\circ \pm \gamma^+$ and $360^\circ - \gamma^+$ are the same as for γ^+ . We found five solutions which span the whole range of γ^+ for $L_{\pm} = \pm 7.5$ and ± 12.5 nm. However, when $L_{\pm} = \pm 25$ and ± 45 nm, only four solutions exist for $\gamma \in (37^\circ, 53^\circ)$, but five for other values of $\gamma^+ \in [0^\circ, 37^\circ] \cup [53^\circ, 90^\circ]$.

For the thickest slab considered, we see from comparing the results presented in Fig. 4(d) with those in Fig. 1(d)—which are same as that for a single metal/SNTF interface—that the two metal/SNTF interfaces are actually uncoupled from each other. The solutions in Fig. 4(d) represent SPP-wave propagation guided by a metal/SNTF interface with the direction of propagation in the xy plane either making an angle γ^+ or γ^- with the morphologically significant plane of the SNTF.

As in Sec. 3.1, the solutions of the dispersion equation can be categorized into three sets with the same criteria as given in Sec. 3.1. However, in this case, the two branches in either of the first two sets do not merge into one branch as L_{met} is increased. Instead,

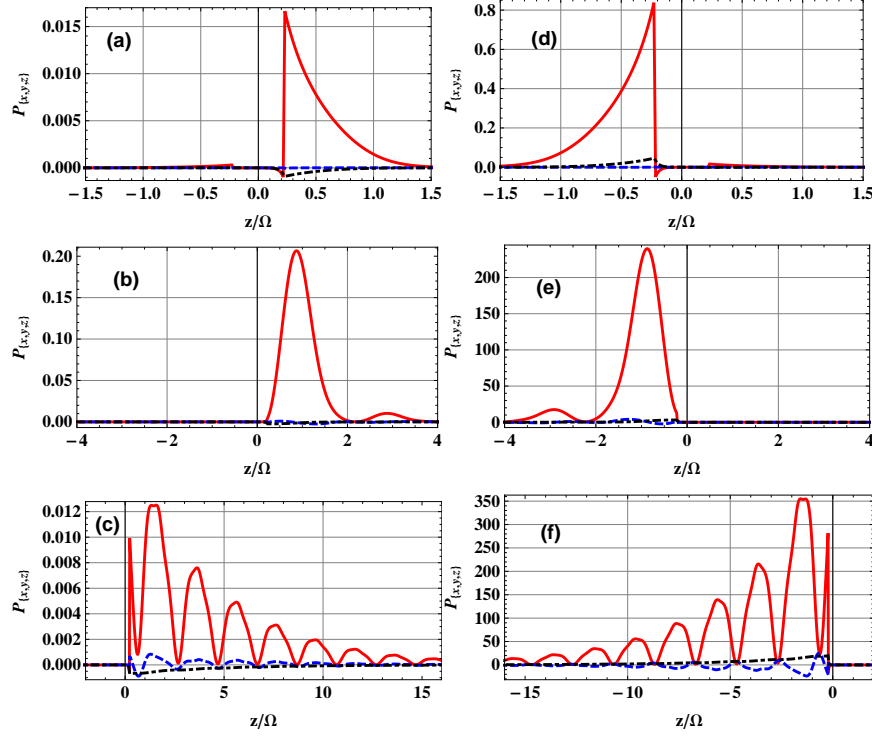


Figure 6. Variation of the Cartesian components of the time-averaged Poynting vector $\mathbf{P}(x, z)$ along the z axis when $x = 0$, $L_{\pm} = \pm 45$ nm, and $\gamma^- = \gamma^+ + 90^\circ$. The following values of κ and γ^+ were chosen to highlight the uncoupling of the two metal/SNTF interfaces, when the metal slab is sufficiently thick. (a-e) $\gamma^+ = 25^\circ$ and (f) $\gamma^+ = 65^\circ$. (a) $\kappa/k_0 = 2.4558 + i0.04214$, (b) $\kappa/k_0 = 2.07725 + i0.003595$, (c) $\kappa/k_0 = 1.8830 + i0.004085$, (d) $\kappa/k_0 = 2.45833 + i0.0424391$, (e) $\kappa/k_0 = 2.06775 + i0.00381762$, and (f) $\kappa/k_0 = 1.8830 + i0.004085$.

the two branches remain distinct, each holding for SPP-wave propagation guided by one of the two metal/SNTF interfaces uncoupled from the other metal/SNTF interface. The single branch in the third set actually vanishes for mid-range values of γ^+ , with the two parts of that branch signifying independent propagation guided by the two metal/SNTF interfaces.

Examination of the field profiles confirms the conclusions made in Sec. 3.1 regarding the effect of the thickness of the metal slab. The asymmetry in the alignment of the morphologically significant planes for $z < L_-$ and $z > L_+$ is reflected in the spatial profiles of the time-averaged Poynting vector presented in Figs. 5 and 6 for $L_{met} = 15$ and 90 nm, respectively. Fig. 5 also suggests that the coupling of the SPP-wave is directly proportional to the real part of wavenumber. So slower SPP waves are more strongly coupled to both interfaces. This observation is also confirmed by the spatial profiles of SPP waves when $L_{met} = 25$ and 50 nm (not shown). Fig. 6 shows the uncoupling of the two metal/SNTF interfaces when the metal slab is sufficiently thick.

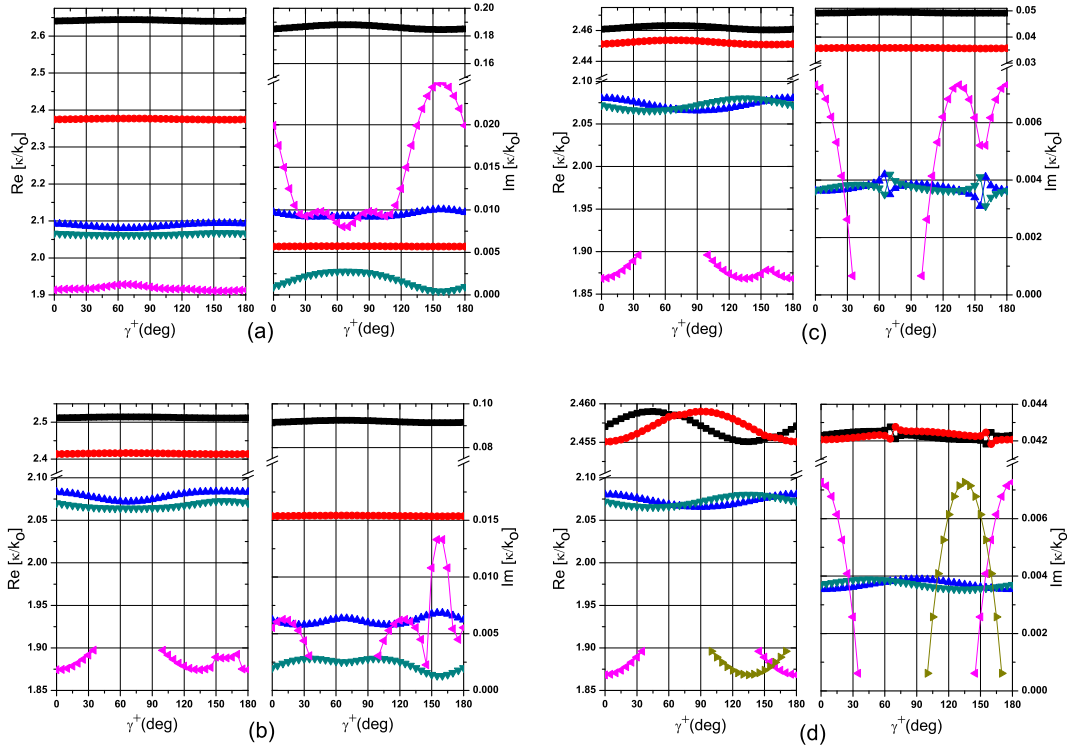


Figure 7. Same as Fig. 1 except $\gamma^- = \gamma^+ + 45^\circ$.

3.3. $\gamma^- = \gamma^+ + 45^\circ$

The solutions of the dispersion equation (25) for $\gamma^- = \gamma^+ + 45^\circ$ are given in Fig. 7 for $\gamma \in [0^\circ, 180^\circ]$. By virtue of symmetry, the solutions for $\gamma^+ + 180^\circ$ are the same as for γ^+ . We found that five solutions exist for the entire range of γ^+ for $L_\pm = \pm 7.5$ nm. When $L_\pm = \pm 12.5$ nm, five solutions exist for $\gamma \in [0^\circ, 37^\circ] \cup [98^\circ, 180^\circ]$ but only four for $\gamma \in (37^\circ, 98^\circ)$. Further thickening of the metal to 50 nm ($L_\pm = \pm 25$ nm) yields five solutions for $\gamma \in [0^\circ, 36^\circ] \cup [99^\circ, 180^\circ]$ but four for $\gamma \in (36^\circ, 99^\circ)$. Decoupling of the two metal/SNTF interfaces becomes very pronounced for $L_\pm = \pm 45$ nm, when all solutions found are the same for either (i) a metal/SNTF interface for which the direction of propagation in the xy plane makes an angle γ^+ with the morphologically significant plane, or (ii) a metal/SNTF interface for which the direction of propagation in the xy plane is inclined at $\gamma^+ + 45^\circ$ to the morphologically significant plane.

Similar to Secs. 3.1 and 3.2, the solutions can be grouped into three sets, with the same criteria given in Sec. 3.1. Representative field profiles for 15-nm- and 90-nm-thick metal slabs are given in Figs. 8 and 9, respectively. We selected one value of κ from each set at $\gamma^+ = 25^\circ$ and 150° . Whereas $\gamma^+ = 25^\circ$ corresponds to the propagation in the xy plane at an angle of 25° with respect to the morphologically significant plane in the region $z > L_+$ and at 70° in the region $z < L_-$, the analogous angles are 30° and 15° , respectively, when $\gamma^+ = 150^\circ$. Fig. 8 shows that SPP waves are guided by

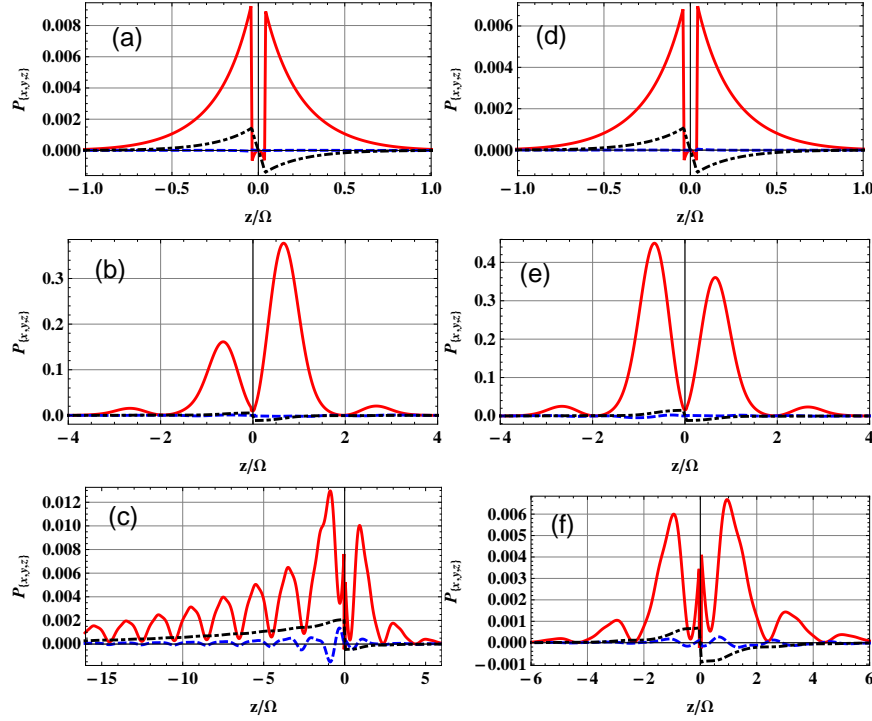


Figure 8. Variation of the Cartesian components of $\mathbf{P}(x, z)$ along the z axis when $x = 0$, $L_{\pm} = \pm 7.5$ nm, and $\gamma^{-} = \gamma^{+} + 45^{\circ}$. (a-c) $\gamma^{+} = 25$, and (d-f) $\gamma^{+} = 150^{\circ}$. (a) $\kappa/k_0 = 2.6423 + i0.1865$, (b) $\kappa/k_0 = 2.08764 + i0.009246$, (c) $\kappa/k_0 = 1.9159 + i0.009486$, (d) $\kappa/k_0 = 2.6398 + i0.1847$, (e) $\kappa/k_0 = 2.09389 + i0.01000$, and (f) $\kappa/k_0 = 1.9108 + i0.02442$.

both interfaces of thin metal slab, but the power density profile is asymmetric due to the fact that morphologically significant planes are not parallel to each other in the two regions occupied by the SNTF. Figure 9 shows that when $L_{met} = 90$ nm, any SPP wave propagates predominantly guided by one of the two metal/SNTF interfaces. We deduce from these two figures that the conclusions drawn in Secs. 3.1 and 3.2 hold true for this case as well, and therefore are general enough.

4. Concluding Remarks

We formulated and solved a canonical boundary-value problem to examine the characteristics of surface-plasmon-polariton waves guided by a thin metal slab inserted in a periodically nonhomogeneous sculptured nematic thin film. The morphologically significant planes on the two sides of the metal slab could be either parallel to or twisted with respect to each other. When the metal slab is very thin, its two interfaces with the SNTF couple to each other, thereby generating more modes of SPP-wave propagation. As the metal slab thickness, the two interfaces decouple. Finally, the two interfaces of a sufficiently thick metal slab independently guide SPP waves.

Acknowledgments. MF thanks the Trustees of the Pennsylvania State University for

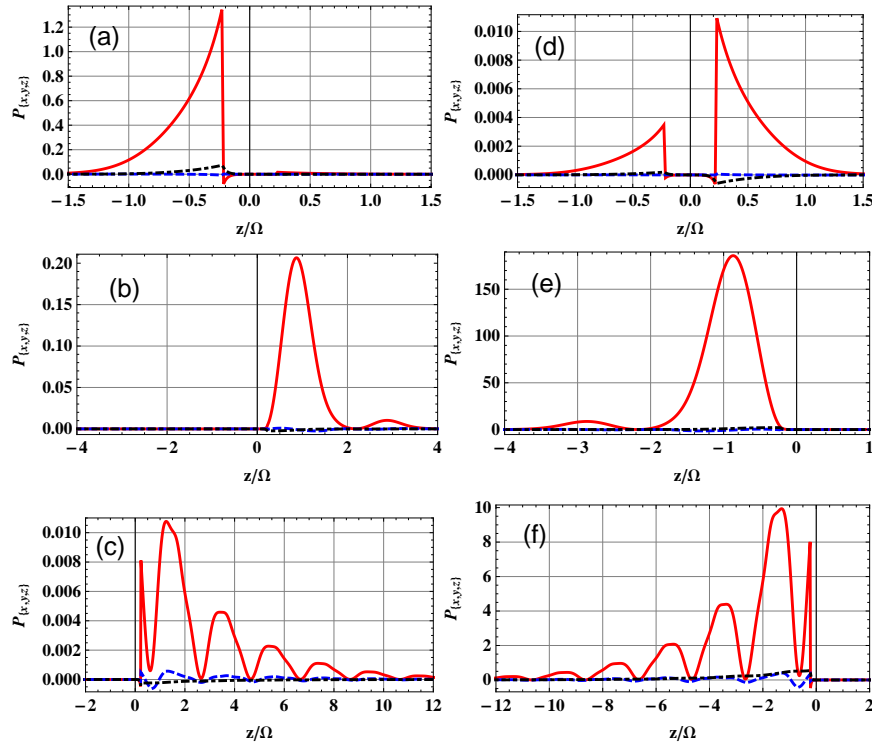


Figure 9. Same as Fig. 8 except that $L_{\pm} = \pm 45$ nm. (a) $\kappa/k_0 = 2.4586 + i0.04246$, (b) $\kappa/k_0 = 2.07725 + i0.003595$, (c) $\kappa/k_0 = 1.8891 + i0.002576$, (d) $\kappa/k_0 = 2.4559 + i0.04227$, (e) $\kappa/k_0 = 2.07916 + i0.003560$, and (f) $\kappa/k_0 = 1.8737 + i0.006143$.

a University Graduate Fellowship. AL is grateful to Charles Godfrey Binder Endowment at the Pennsylvania State University for partial support of this work.

References

- [1] Zayats A V, Smolyaninov I I and Maradudin A A 2005 *Phys. Rept.* **408** 131
- [2] Maier S A 2007 *Plasmonics: Fundamentals and Applications* (New York: Springer)
- [3] Felbacq D 2008 *J. Nanophoton.* **2** 020302
- [4] Polo Jr J A and Lakhtakia A 2010 *Laser Photon. Rev.* doi:10.1002/lpor.200900050
- [5] Homola J (ed) 2006 *Surface Plasmon Resonance Based Sensors* (Heidelberg: Springer)
- [6] Kalele S A, Tiwari N R, Gosavi S W and Kulkarni S K 2007 *J. Nanophoton.* **1** 012501
- [7] Abdulhalim I, Zourob M and Lakhtakia A 2008 *Electromagnetics* **28** 214
- [8] Dragoman M and Dragoman D 2008 *Prog. Quantum Electron.* **32** 1
- [9] Abdulhalim I, Zourob M and Lakhtakia A 2007 *Handbook of Biosensors and Biochips* ed R Marks, D Cullen, I Karube, C R Lowe and H H Weetall (Chichester: Wiley) pp 41346
- [10] Aoki U, Shimada K, Nagano M, Kawai M and Koga H 2005 *Proteomics* **5** 2396
- [11] Kanda V, Kitov P, Budle D R and McDermott M T 2005 *Anal. Chem.* **77** 7497
- [12] Kik P G, Maier S A and Atwater H A 2002 *MRS Symp. Proc.* **705** Y3.6
- [13] Maier S A, Brongersma M L, Kik P G, Meltzer S, Requicha A A G and Atwater H A 2001 *Adv. Mater.* **13** 1501
- [14] Berini P 2009 *Adv. Opt. Photon.* **1** 484
- [15] Jen Y J, Lakhtakia A, Yu C W and Chan T Y 2009 *J. Opt. Soc. Am. A* **26** 2600
- [16] Polo Jr J A and Lakhtakia A 2009 *Proc. R. Soc. Lond. A* **465** 87

- [17] Motyka M A and Lakhtakia A 2009 *J. Nanophoton.* **3** 033502
- [18] Mackay T G and Lakhtakia A 2010 *Electromagnetic Anisotropy and Bianisotropy: A Field Guide* (Singapore: World Scientific)
- [19] Lakhtakia A 2002 *Mater. Sci. Engg. C* **19** 427
- [20] Lakhtakia A and Messier R 2005 *Sculptured Thin Films: Nanoengineered Morphology and Optics* (Bellingham, WA: SPIE Press).
- [21] Motyka M A and Lakhtakia A 2008 *J. Nanophoton.* **2** 021910
- [22] Faryad M, Polo Jr J A and Lakhtakia A 2010 *J. Nanophoton.* **4** 043505
- [23] Lakhtakia A, Jen Y-J and Lin C-F 2009 *J. Nanophoton.* **3** 033506
- [24] Polo Jr J A and Lakhtakia A 2009 *Proc. R. Soc. Lond. A* **465** 87
- [25] Devender, Pulsifer D P and Lakhtakia A 2009 *Electron. Lett.* **45** 1137
- [26] Economou E N 1969 *Phys. Rev.* **182** 539
- [27] Wendler L and Haupt R 1987 *Phys. Status Solidi B* **143** 131
- [28] Yang F, Sambles J R and Bradberry G W 1991 *Phys. Rev. B* **44** 5855
- [29] Faryad M and Lakhtakia A 2010 *Phys. Status Solidi RRL* doi: 10.1002/pssr.201004049
- [30] Agarwal K, Polo Jr J A and Lakhtakia A 2009 *J. Opt. A: Pure Appl. Opt.* **11** 074003
- [31] Yakubovich V A and Starzhinskii V M 1975 *Linear Differential Equations with Periodic Coefficients* (New York: Wiley)
- [32] Hodgkinson I J, Wu Q H and Hazel J 1998 *Appl. Opt.* **37** 2653
- [33] Jaluria Y 1996 *Computer Methods for Engineering* (New York: Brunner-Routledge)